STU
SLOVAK UNIVERSITY OF TECHNOLOGY IN BRATISLAVA

Journal of Electrical Engineering, Vol. 77, No. 2, 2026, pp. 189-199
https://reference-global.com/journal/JEE

# Acoustic noise prediction for synchronous motors with different topologies using MFCC-based datasets

**Faaris Mujaahid, Min-Fu Hsieh*, Thorikul Huda**

Unpleasant acoustic noise from electric machines not only affects human perception but also serves as a potential indicator of underlying mechanical or electromagnetic issues. From an electromagnetic perspective, this noise primarily originates from radial electromagnetic forces acting on the stator and rotor structures. This paper presents a novel framework that integrates deep learning with multiphysics system modeling to predict and classify the conditions of permanent-magnet motors based on Mel-frequency cepstral coefficient (MFCC)-derived acoustic datasets. Measured acoustic data from a target motor are compared with simulated results obtained through finite element analysis (FEA), with waterfall diagrams demonstrating high correlation between experiment and simulation. Literature shows limited coverage of integrated methods that couple multiphysics-based dataset generation with neural-network training for acoustic-noise prediction. The FEA-based simulation process enables efficient generation of 2,640 labeled datasets within 470 hours, representing four motor conditions: reference, adjusted magnet size, adjusted air gap, and combined magnet-air-gap adjustment. Using these datasets, a trained neural network achieves a classification accuracy of 95.68%, successfully identifying the causes of motor design deviations through acoustic-noise features for further design improvements.

Keywords: NVH, neural network, acoustic noise, synchronous motor, FEA

## 1 Introduction

Environmental pollution, global warming, depletion of fossil fuels, and the need for energy efficiency have heightened interest in electric vehicles (EVs) due to their low fuel consumption, quiet operation, and low maintenance costs. A critical aspect of this development is the improvement of electric propulsion motors, which are essential components of EVs [1]. These electric machines should meet performance and reliability standards, featuring high torque/power density, a wide speed range, overload capacity, high efficiency at all speeds, rapid acceleration and deceleration, low cost and weight, durability in harsh conditions, long lifespan, and low vibration and noise. The main types of electric machines potentially utilized in electric vehicles include induction motors (IMs), permanent magnet (PM) synchronous motors (PMSMs), switched reluctance motors (SRMs), and synchronous reluctance motors (SynRMs) [2].

While SRMs and SynRMs hold promise for mitigating the cost fluctuations and material scarcity linked to permanent magnets, IMs and PMSMs continue to dominate propulsion systems in Plug-in Electric Vehicles (PEVs) [3, 4]. IMs feature a magnet-less design and operate through the rotation of an induced magneto-motive force (MMF). Their advantages include simplicity, cost-effectiveness, broad speed range, robustness, reliability, and favorable dynamic performance [4].

In contrast, PM machines are recognized for their high efficiency, superior torque density, compact size, and lightweight design, making them the preferred choice for EV traction motors [3, 5].

Without careful design, acoustic noise and vibration can pose significant challenges in PMSMs [6-7]. Research identifies radial forces as the main electromagnetic contributors to Noise, Vibration, and Harshness (NVH) [8]. Assessing the noise levels of PMSMs allows for early detection and mitigation of potential issues before prototype manufacturing. Key factors influencing NVH include the magnetic force of the permanent magnet and the stator-housing's natural frequencies [9]. Noise reduction strategies suggest optimizing slot/pole combinations [10], stator yoke thickness and teeth shape [9], and rotor topology [11]. Reducing noise levels in PM machines is achieved primarily by increasing stator yoke stiffness and reducing dominant electromagnetic forces [12].

Despite progress in reducing audible noise through design improvements, further advancements in motor design and acoustic noise assessment are possible with machine learning (ML) techniques. Few studies have explored the application of ML in electric motor design. Cai et al. [13] proposed an offline and online-trained Radial Basis Function (RBF) neural network model to estimate the SRM flux linkage under dynamic operating

Department of Electrical Engineering, National Cheng Kung University, Tainan City, Taiwan
mfhsieh@mail.ncku.edu.tw

https://doi.org/10.2478/jee-2026-0020, Print (till 2015) ISSN 1335-3632, On-line ISSN 1339-309X

conditions. In another study, Nogay investigated the application of a Deep Convolutional Neural Network (DCNN) to estimate the stator coil pitch of an induction motor from current signals, achieving 100% operational accuracy [14]. Hsieh et al. [15] provided a combined approach of ML and equivalent magnetic circuit analysis to design a surface-mounted permanent magnet synchronous motors (SPMSMs) for simulation-free purpose. ML has also been applied for fault diagnosis related to motor geometry [16], faults detection [17, 18], accuracy and loss prediction [19], and as an alternative to finite element analysis (FEA) for motor vibration suppression [20].

While some research has applied ML to fault diagnosis and performance prediction in electric motor design and optimization, few studies have specifically addressed vibration and noise performance using a combined approach of FEA and machine learning or deep learning. Therefore, the primary objective of this paper is to establish a framework that integrates machine learning/deep learning with multiphysics system modeling to predict IPMSM conditions using thousands of simulated noise datasets. The proposed predictive model framework facilitates efficient and cost-effective electric motor development by utilizing noise data generated through coupled experimental and FEA methods, emphasizing a straightforward, rapid, and simplified measurement setup based on audio recordings.

The developed acoustic-based analysis framework represents a practical and cost-efficient alternative to conventional vibration-based diagnostic systems, which typically rely on integrated data logging instruments such as vibration meters and accelerometers. By leveraging both experimental audio measurements (via microphone and soundcard setup) and simulation-based motor modeling for dataset generation and machine-learning training, the framework demonstrates comparable diagnostic accuracy while significantly lowering instrumentation and operational costs.

The following sections are structured as follows: Section 2 covers noise sources and mechanisms in electric motors. Section 3 discusses motor specifications, experimental-simulation methodology, and the classifier algorithm. Section 4 presents the results and discussion; and the final section provides the conclusion.

## 2 Vibration and acoustic noise mechanism

### *2.1. Source of noise*

Figures 1 and 2 illustrate the sources, transmission paths, and mechanisms of vibration and acoustic noise in electric machines. In interior permanent magnet synchronous motors (IPMSMs), multiple sources contribute to overall noise, including electromagnetic, mechanical, and aerodynamic factors. Electromagnetic noise originates from radial and tangential electromagnetic forces as well as power converter switching effects. The interaction between the radial and tangential components of the magnetic flux density within the air gap produces tangential force density, which generates torque, and radial harmonic forces that excite structural vibration [21, 22]. These radial and tangential components can be further influenced by factors such as improper assembly, manufacturing defects, or shaft misalignment and bending, all of which induce mechanical vibration [23]. Bearing-related problems, including misalignment, imbalance, wear, or corrosion, as well as loose fasteners and rotor-stator eccentricity, also exacerbate vibration and amplify electromagnetic-mechanical coupling noise. Additionally, airflow within the narrow gap between the rotor and stator produces aerodynamic noise, which manifests as audible acoustic emissions. Collectively, these electromagnetic, mechanical, and aerodynamic sources excite structure-borne vibration that transfers energy to the surrounding air, ultimately resulting in acoustic noise.

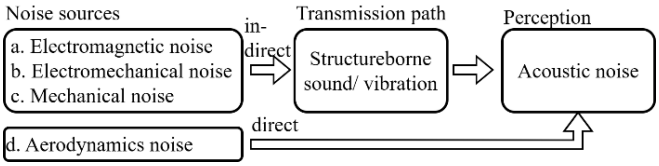


**Fig. 1.** Typical vibration and noise in PMSMs

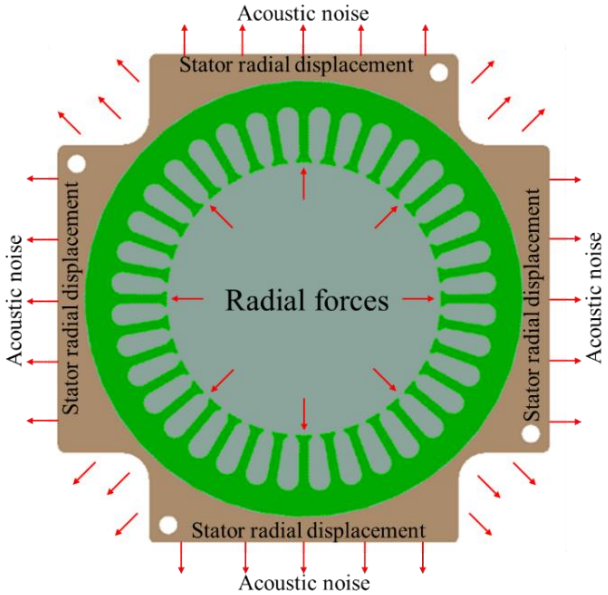


**Fig. 2.** Mechanism of generating vibration and noise in IPMSMs

### *2.2 IPMSM radial flux*

Radial electromagnetic forces contribute more significantly to acoustic noise in electric machines due to the stator frame assembly's lower stiffness in the radial direction compared to the tangential direction. This structural difference causes the stator to be more susceptible to radial deformation under strong radial forces generated by electromagnetic interactions between the rotor and stator. Consequently, these radial displacements induce vibrations that propagate as acoustic noise, impacting overall machine performance [24-27]. The radial and tangential force densities can be expressed, respectively, as

$$\mathbf{F_{rad}}(t,\alpha) = \frac{1}{2\mu_0}\left(\mathbf{B_{rad}}^2(t,\alpha) - \mathbf{B_{tan}}^2(t,\alpha)\right) \quad (1)$$

$$\mathbf{F_{tan}}(t,\alpha) = \frac{1}{\mu_0}\mathbf{B_{rad}}^2(t,\alpha).\mathbf{B_{tan}}^2(t,\alpha) \quad (2)$$

where $\mathbf{F_{rad}}$ and $\mathbf{F_{tan}}$ are radial and tangential force densities, respectively, $\mathbf{B_{rad}}$ and $\mathbf{B_{tan}}$ are radial and tangential flux densities, respectively, both being function of time $t$, and the circumferential position $\alpha$ of the stator. Parameter $\mu_0$ represents the air permeability.

To sum up, the harmonics of the radial force component are the primary cause of stator vibration, while the harmonics of the tangential force component mainly lead to torque ripple.

The air-gap flux density varies periodically in both time and space, and consequently, the electromagnetic force exhibits distinct spatiotemporal distribution characteristics. In general, the electromagnetic force $P_n$ can be expressed as a superposition of a series of rotating waves with different frequencies and spatial orders, given as [28]

$$P_n(\theta,t) = \sum_m P_m \cos\left(\omega_m t - m\theta + \phi_m\right) \quad (3)$$

where $P_m$ denotes the amplitude of the electromagnetic force with specific spatial order $m$, angular frequency $\omega_m$, and phase angle $\phi_m$.

Resonance in PMSMs, leading to significant vibration and noise, occurs under two conditions [28]: (a) when the spatial order of electromagnetic force matches the natural mode's circumferential order, and (b) when the force frequency nears the modal frequency. Radial-flux motors primarily radiate noise from the annular housing, while axial-flux motors do so from the disk cover. These PMSMs differ in modal characteristics, creating distinct vibration and noise mechanisms.

To identify the electromagnetic forces acting on PMSMs under different operating conditions, this study leverages finite element analysis (FEA) to simulate force distributions for various load and speed scenarios. By varying the input conditions in the FEA model, the dynamic electromagnetic interactions and their impact on radial forces can be analyzed.

## 3 Measurement setup, simulated data collection and classifier algorithm

The workflow of the proposed method is depicted in Fig. 3. As shown, the flowchart illustrates a systematic approach to developing an acoustic-noise predictive system for IPMSMs, utilizing deep learning and FEA simulations validated against experimental measurements. In Fig. 3, yellow, blue, and green boxes represent measurement data, FEA-collected data, and the deep-learning algorithm, respectively. Note that the validation step in the middle of the flowchart (i.e., after obtaining the experimental and simulation data) primarily serves to demonstrate the reliability of the simulations.

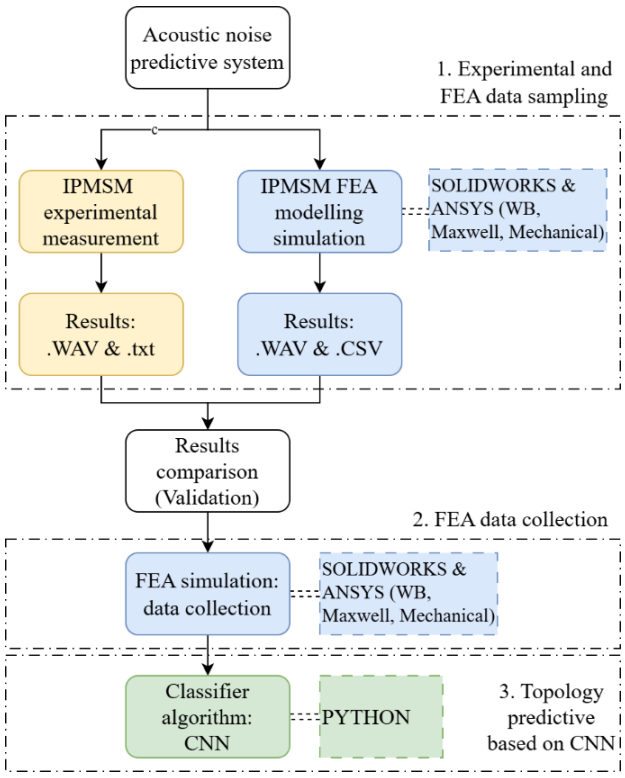


**Fig. 3.** Proposed framework combining Multiphysics modelling and deep learning

The proposed framework primarily utilizes acoustic noise data as the input for performance prediction, rather than relying on direct vibration measurements. Although vibration data and their collection methods (axial or radial) are critical in related studies, they are beyond the scope of this work. The focus here is on using readily available and low-cost tools, such as microphones, soundcards, and computers, for audio data acquisition. Furthermore, the proposed approach does not directly assess performance variations caused by changes in

speed or load. Instead, it emphasizes model training and output generation under predefined operating conditions, with speed and load variations incorporated through FEA.

### *3.1 Motor specification*

A 3.7 kW IPMSM is used for experimental validation and as a simulation model of finite element analysis. Motor specifications are summarized in Tab. 1.

**Table 1.** IPMSM specifications

| Item | Value/Unit |
|---|---|
| Rated power | 3.7 kW |
| Rated & max torque | 11.78 Nm & 29.4 Nm |
| Rated voltage | 220 V |
| Rated and max current | 18.5 $A_{rms}$ & 45 $A_{rms}$ |
| Rated speed | 3000 RPM |
| Number of poles | 8 |
| Inertia | 0.00633 kg.m$^3$ |
| $L_d/L_q$ | 0.76 mH/1.61 mH |
| Resistance of stator windings | 141.6 mΩ |
| Flux linkage | 80 mWb |
| Magnet (m) length × width | 5 mm × 29.5 mm |
| Airgap (Ag) | 0.9 mm |
| Rotor outer diameter | 98.2 mm |
| Stator inner diameter | 100 mm |
| Stator outer diameter | 160 mm |

### *3.2 Measurement setup*

Figure 4 (a) illustrates the experimental setup used to generate and capture acoustic noise from the 3.7 kW electric machine ADLEE MA-3700M (Fig. 4 (b)) driven by a three-phase Delta Electronics C2000 driver. Acoustic measurements are collected using an ECM8000 Behringer microphone connected to a UMC202HD Behringer soundcard via an XLR cable, positioned 50 cm from the motor, as shown in Fig. 4 (c). The collected digital data is processed in LabVIEW, producing a frequency-dB contour plot for 21 speed points, ranging from 1000 RPM to 3000 RPM in 100 RPM increments. This experimental procedure serves to confirm that the frequency-domain simulation results align closely with empirical data, thereby validating the accuracy of the FEA simulations conducted in this study.

The proposed framework in Fig. 3 consists of three sequential stages. The first stage acquires sample data from both experimental measurements and finite element analysis simulations conducted under identical parameters and boundary conditions. The second stage, following an initial quantitative comparison between the

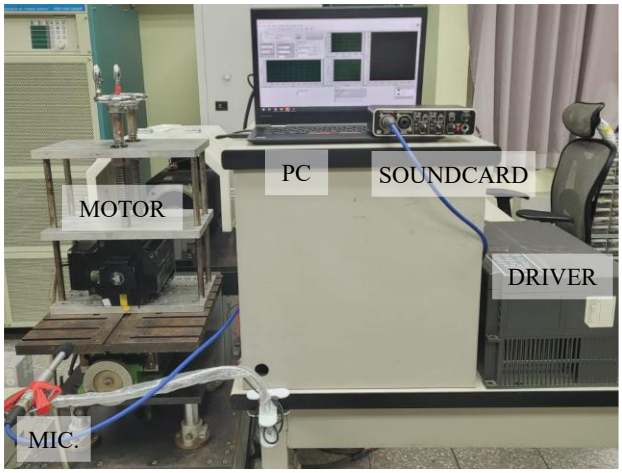


(a)

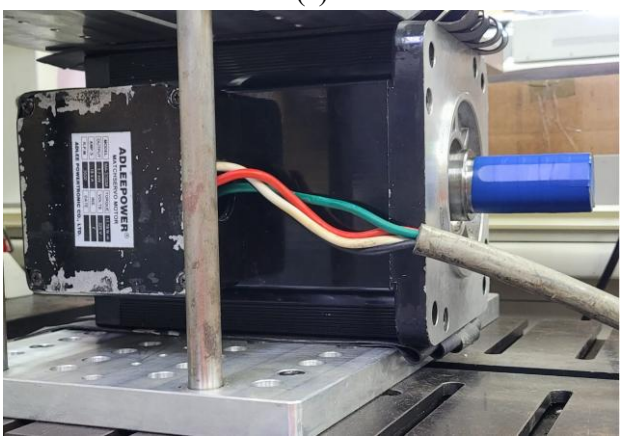

(b)

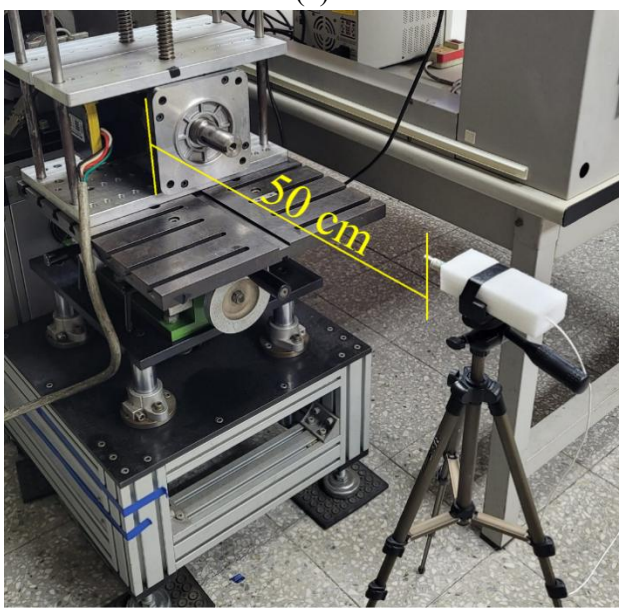


(c)

**Fig. 4.** (a) Experimental setup as illustrated in upper left block diagram of Fig. 3 *IPMSM experimental measurement*, (b) the 3.7 kW motor under test, (c) positioning of microphone towards the electric motor to capture the emitted noise.

measured and simulated data, expands the dataset through additional simulations that encompass a wider range of operating conditions, including variations in speed, load, and motor topology. This process substantially reduces the time required to collect hundreds or even thousands of audio samples compared with experimental measurements. The third stage uses the large dataset obtained in the previous step to train a classification model that predicts motor conditions based on the acquired audio signals in the Waveform Audio File (WAV) format.

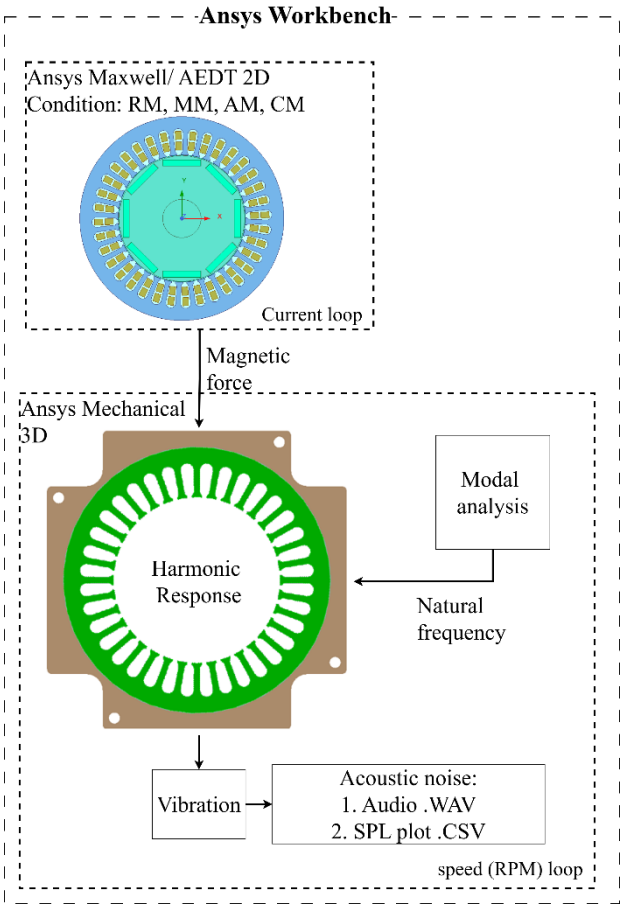


**Fig. 5.** Flowchart of coupled FEA and CNN analysis

### *3.3 Simulated data collection*

The FEA modeling, represented partially by the blue boxes in Fig. 3 and detailed further in Fig. 5, involves two primary processes conducted within Ansys Workbench: Ansys Maxwell and Ansys Mechanical.

The electromagnetic analysis of the target 8-pole IPMSM is performed using two-dimensional simulations with Ansys Maxwell to calculate the electromagnetic forces. These forces are subsequently transferred to Ansys Mechanical, where harmonic response and modal analysis are employed to generate the corresponding acoustic noise. This process produces WAV and Comma-Separated Values (CSV) data, which are further utilized in a neural network (NN) algorithm as the data source for analyzing the acoustic noise and predicting the motor condition.

In FEA, creating an optimal mesh design requires balancing accuracy and computational efficiency. This balance is typically achieved through a mesh refinement study, which involves progressively increasing the mesh density or reducing the element size while monitoring variations in the analysis outcomes. When the results stabilize and exhibit minimal changes with further refinement, the analysis is considered mesh-independent [29-32]. In Ansys Mechanical, achieving mesh independence is crucial to ensure accurate results while maintaining computational efficiency. Detailed parameters used in this work can be found in a previous publication [33]. Based on the balance between accuracy and computational efficiency illustrated and discussed in [33], a hexahedral mesh with an element size of 10 mm is selected to meet the mesh requirement.

### *3.4 Experimental validation of acoustic simulations*

Comparison between the experimental measurements and the FEA modeling of the IPMSM is performed once for each motor model. Experimental measurement is essential to validate the simulation results. Although experimental testing is time-consuming, it can be complemented by modeling and simulation to efficiently generate a larger number of audio datasets. However, the simulation results should be compared with the experimental ones, for instance, through a waterfall diagram, as illustrated in Fig. 6.

Figure 6 presents a comparison between the experimental and simulation results, displaying three-dimensional data: frequency (Hz), motor speed (RPM), and sound pressure level (SPL, dB). In Figs. 6 (a) and 6 (b), two distinct trends are highlighted by the red and black arrows. The first yellowish band starts at approximately 500 Hz and 1,000 RPM, as indicated by the lower red arrow, and extends to around 1,700 Hz and 3,000 RPM, marked by the upper red arrow. The second band begins near 1,250 Hz and 1,000 RPM, indicated by the lower black arrow, and concludes at 3,000 Hz and approximately 2,500 RPM, as shown by the upper black arrow. Although the lines in Fig. 6 (a) are not perfectly aligned, a noticeable similarity with Fig. 6 (b) can still be observed. This comparison validates the motor model by demonstrating that the simulated acoustic noise generated through FEA closely corresponds to the behavior of the actual motor. Nonetheless, certain limitations exist in the experimental measurements, particularly due to interference from external ambient noise captured during the acoustic recordings.

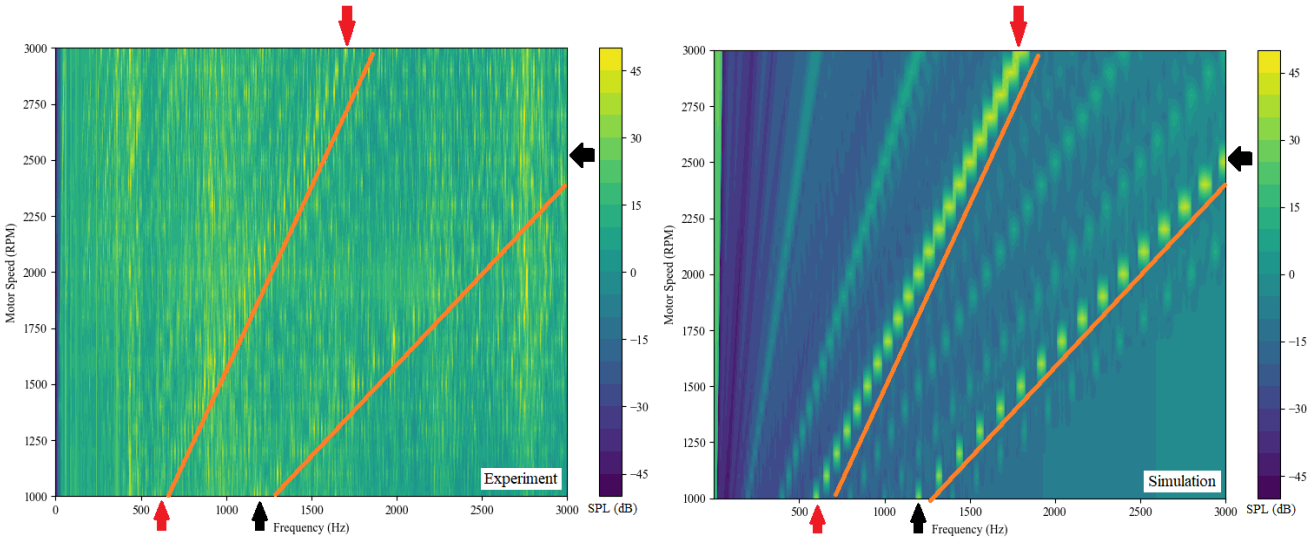


(a) (b)

**Fig. 6.** Comparison between (a) experimental measurement and (b) simulation result at no load, speed 1000 RPM to 3000 RPM. The sound pressure level (SPL, in dB) is identified by a colour gradient, dark purple (-45 dB) to yellow (45 dB) colour gradient. An orange auxiliary line is added to point out the similarity between both (a) and (b).

### *3.5 Classifier and convolutional neural network*

A classifier algorithm enables rapid inference of motor conditions. Due to time constraints and the limited capabilities of FEA tools, machine-learning approaches provide a more effective and practical means for predicting motor conditions.

The classification algorithm employs a Convolutional Neural Network (CNN) as the predictive model, whose structural architecture is illustrated in Fig. 7.

The input consists of JSON-formatted data extracted from WAV audio files, which are subsequently converted into 39-frame mel-frequency cepstral coefficients (MFCC) for two-time segments. This segmentation approach effectively expands the dataset to 5,280 samples, as summarized in Tab. 2. The cepstral features are computed from the sound pressure level (SPL) according to the following formulation [34]:

$$C(x(t)) = F^{-1}[\log(F[x(t)])] \qquad (4)$$

where the cepstrum $C$ (dB) is calculated by applying the inverse Fourier Transform F-1 to the logarithm of the magnitude spectrum derived from the Fourier Transform $F[x(t)]$, in which $x(t)$ represents the time-domain SPL (dB). Within the CNN framework, the cepstrum serves as the feature extraction mechanism, converting the WAV audio signals into numerical representations stored in JSON format for subsequent processing.

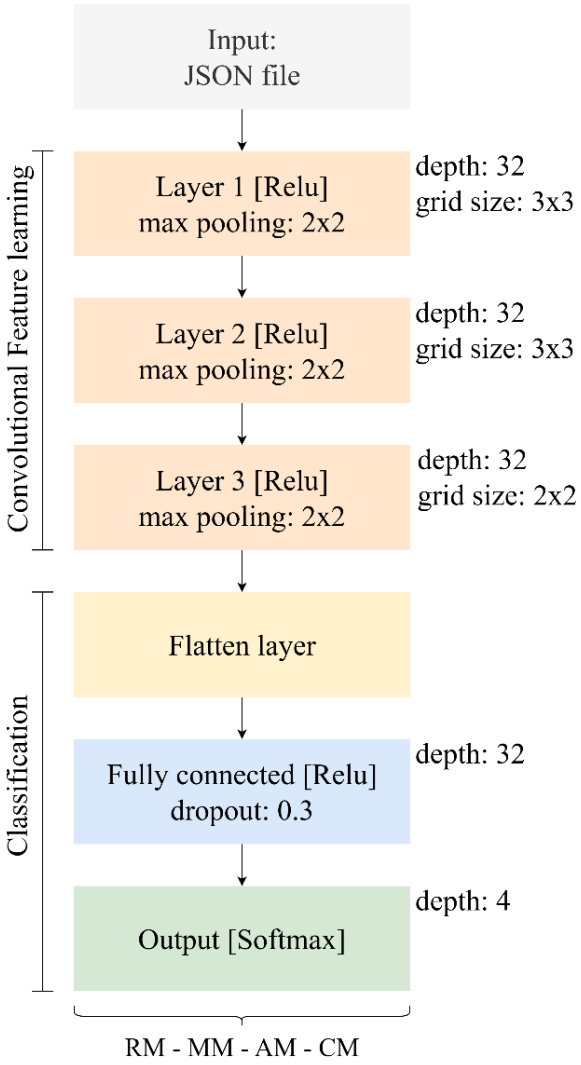


**Fig. 7.** CNN architecture

A total of 2,640 samples, categorized under four distinct operating conditions (RM, MM, AM, and CM) as detailed in Tab. 2, are used to train the CNN model. During the training process, the network learns to recognize the characteristic patterns associated with each condition. After completing the training and validation phases, unseen samples are presented to the model for classification, as shown on the lower side of Fig. 7. The model architecture consists of three convolutional layers, each followed by a max-pooling operation for spatial downsampling. The first three hidden layers, together with the fully connected layer, employ the Rectified Linear Unit (ReLU) activation function, whereas the output layer utilizes the Softmax function. These activation functions are mathematically defined for ReLU and Softmax, respectively, as given by [35]

$$f(a) = \begin{cases} a, & a \geq 0 \\ 0, & a \leq 0 \end{cases} \tag{5}$$

$$\sigma(b_i) = \frac{e^{b_i}}{\sum_{j=1}^{n} e^{b_j}} \tag{6}$$

where $f(a)$ and $y$ denote the output and input, respectively. For positive values, $f(a)=a$ increases linearly with a slope of 1, whereas for negative inputs, $f(a)=0$, consistent with the behavior of the ReLu. The Softmax function, on the other hand, transforms a vector of raw model output (logit, $\sigma$) into a probability for multi-class classification, where $b_i$ and $n$ represent the *i-th* logit for a given class and the total number of classes, respectively.

The kernel depths and corresponding pixel dimensions for each layer are detailed in Fig. 7. The training configuration consists of 100 epochs, utilizing the Adam optimization algorithm with a fixed learning rate of 0.0001 [36-37].

## 4 Results and discussion

As mentioned previously, to train the neural network for vibration and acoustic noise prediction in IPMSMs, a dataset of 2,640 samples was generated through finite element analysis using Ansys Maxwell and Ansys Mechanical. Each dataset includes two outputs, a WAV file and a CSV file, which respectively provide the acoustic signal and corresponding numerical data for subsequent analysis and model training.

### *4.1 Training result validation*

Figures 8 and 9 illustrate the training and validation accuracy of the CNN model over 100 epochs, using a dataset split of 60% for training, 15% for validation, and 25% for testing. The model exhibits a steady improvement in accuracy, stabilizing around epoch 40, with a final training accuracy of 95.68% and a training loss of 0.0709. Validation accuracy similarly reaches 96.34%, with a validation loss of 0.1282, demonstrating strong generalization capability. After epoch 40, both accuracy and loss curves flatten, indicating convergence and near-optimal performance. The close alignment between training and validation curves further confirms that the model is well-fitted and free from significant overfitting.

**Table 2.** Dataset condition of acoustic noise

| Dataset class | Condition | Number of data |
|---|---|---|
| Reference model (RM) | 1. 11 varying currents $I_{rms}$ respectively: 0 A (no load), 5 A, 10 A, 15 A, 18.5 A (rated), 20 A, 25 A, 30 A, 35 A, 40 A, 45 A (max)<br>2. 100 RPM increment from 100 to 6,000, equals to 60 different speeds. | 660 |
| Adjusted magnet model (MM) | 1. Magnet size is reduced to 3 mm × 25 mm.<br>2. 11 varying $I_{rms}$ and 60 varying RPM as applied in RM | 660 |
| Adjusted airgap model (AM) | 1. Airgap is increased to 2 mm.<br>2. 11 varying $I_{rms}$ and 60 varying RPM as applied in RM | 660 |
| Combined magnet & airgap model (CM) | 1. Combining MM and AM conditions:<br>a. Magnet size is reduced to 3 mm × 25 mm.<br>b. Airgap is increased to 2 mm.<br>2. 11 varying $I_{rms}$ and 60 varying RPM as applied in RM. | 660 |
| TOTAL | | 2,640 |

The confusion matrix shown in Fig. 10 summarizes the classification performance across the four conditions: RM, MM, AM, and CM, with detailed values listed in Tab. 3. The model achieves consistently high accuracy, particularly for RM and MM. For RM, 309 samples are correctly classified, while 15 are misclassified as MM, resulting in an accuracy of 95.37%. For MM, 322 samples are correctly classified and 6 are misclassified as RM, yielding an accuracy of 97.87%. Class AM shows 315 correct and 16 misclassified samples (as CM), whereas CM records 317 correct and 20 misclassified samples (as AM), corresponding to

accuracy of 95.12% and 94.07%, respectively. The confusion between AM and CM indicates that the model encounters greater difficulty distinguishing between these two conditions, likely due to the influence of airgap variations associated with the smaller rotor diameter in AM. Overall, the model demonstrates robust classification performance and reliable generalization across all operating conditions.

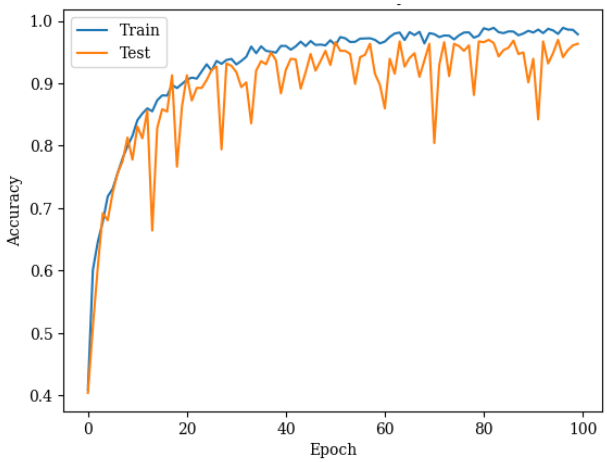


**Fig. 8.** CNN model accuracy

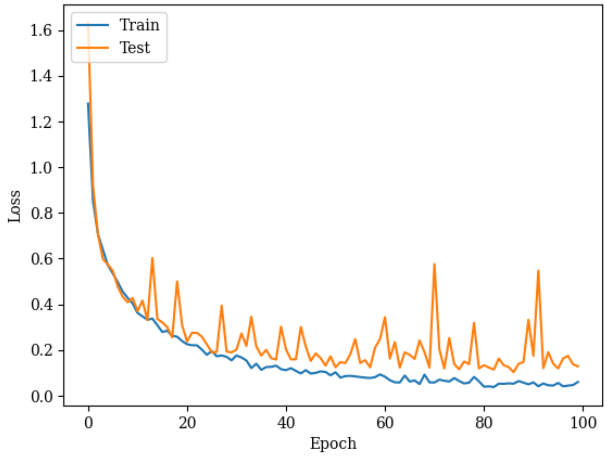


**Fig. 9.** CNN model loss

The total simulation process is divided into two stages. In the first stage, 2,640 datasets are generated. For each applied current across 60 speeds, it takes 10.67 hours to produce 60 CSV files (61 kB each) and corresponding 10-second WAV files (1.7 MB each). With 11 current levels per condition, approximately 117.37 hours are required to create 660 CSV and WAV files. Consequently, generating all 2,640 datasets under four conditions requires 469.48 hours in total. This duration is considerably shorter than that of experimental data collection, which demands greater time, energy, and cost, and carries a risk of hardware damage. The simulation time can be further reduced by employing a high-performance computer and automating the workflow. The second stage, involving CNN classifier training with the 2,640 datasets, requires 1.5 hours.

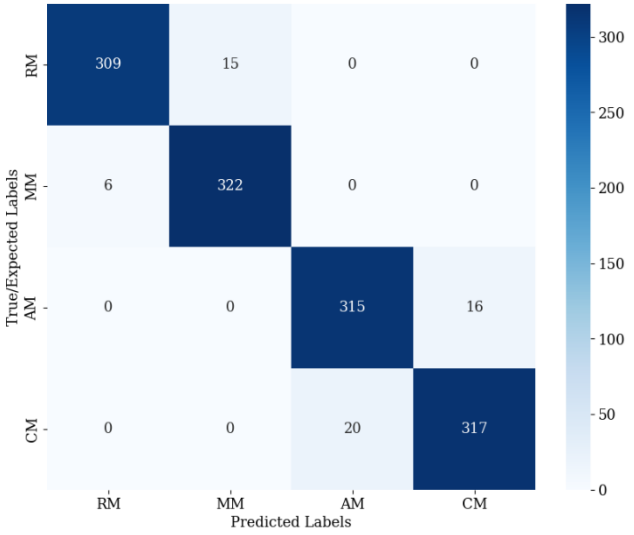


**Fig. 10.** Confusion matrix

**Table 3.** Summary of confusion matrix

| Condition | Correct prediction | Misclassified as | | | |
|---|---|---|---|---|---|
| | | RM | MM | AM | CM |
| RM | 309<br>95.37% | | 15<br>4.63% | 0 | 0 |
| MM | 322<br>98.17% | 6<br>1.83% | | 0 | 0 |
| AM | 315<br>95.12% | 0 | 0 | | 16<br>4.83% |
| CM | 317<br>94.07% | 0 | 0 | 20<br>5.93% | |
| Total correct prediction | | | | | 1,263<br>95.68% |
| Total misclassification | | | | | 57<br>4.32% |

The evaluation metrics summarized in Tab. 4 indicate that the proposed CNN model achieves consistently high performance across all four operating conditions. The RM and MM classes show the best results, each attaining an F1-score of 0.97, supported by strong precision and recall values (0.98/0.95 for RM and 0.96/0.98 for MM, respectively). These findings confirm the model's ability to accurately identify both normal and early-stage malfunction patterns. The AM and CM classes, while slightly lower in performance, still maintain robust F1-scores of 0.95, with precision values of 0.94 and 0.95, respectively, indicating a minor increase in false positives compared to RM and MM. As each class contains a balanced number of samples: 324, 328, 331, and 337 for RM, MM, AM, and CM, respectively, the evaluation results are considered statistically reliable.

**Table 4.** Summary of evaluation matrix

| Condition | Precision | Re-Call | F1-Score |
|---|---|---|---|
| RM | 0.98 | 0.95 | 0.97 |
| MM | 0.96 | 0.98 | 0.97 |
| AM | 0.94 | 0.95 | 0.95 |
| CM | 0.95 | 0.94 | 0.95 |

### *4.2 Discussion*

The results demonstrate that the proposed CNN model achieves high classification accuracy and strong generalization capability across all four operating conditions. The convergence behaviour of the training and validation curves (Figs. 8 and 9) indicates a well-optimized learning process with minimal overfitting. The model stabilizes after approximately 40 epochs, suggesting efficient feature extraction and convergence toward optimal-weight configurations. The close agreement between training and validation accuracies (95.68% and 96.34%) further confirms the model's robustness and adaptability to unseen data.

Analysis of the confusion matrix and cross-validation results (Fig. 10 and Tabs. 3 and 4) corroborates the model's reliability. The highest accuracies are observed for the RM and MM classes, reflecting the model's effectiveness in detecting normal and mild malfunction states. The relatively higher number of misclassifications between AM and CM indicates that these conditions exhibit overlapping acoustic or vibration features, primarily due to airgap-related effects. Nevertheless, both classes maintain accuracies exceeding 94%, demonstrating strong discriminative capability and consistent overall performance.

These results suggest that the proposed method can further serve as a guide for improving motor design.

## 5 Conclusion

This study presented an efficient framework for motor-performance prediction and acoustic-noise data generation, with FEA-simulated results validated against experimental measurements using waterfall diagrams. A CNN trained on 2,640 samples achieved training and validation accuracies of 95.68% and 96.34%, respectively. Testing across four conditions also yielded high accuracy, with RM, MM, AM, and CM achieving 95.37%, 98.17%, 95.12%, and 94.07%. Among 1,320 test samples, only 57 were misclassified, primarily between AM and CM, indicating strong classification robustness and minimal overfitting. Taken together, these results indicate that the proposed method can also serve as an indicator and practical guide for motor design improvements. Future work will involve anechoic chamber measurements to refine spectral resolution, automation to minimize manual intervention, and extension of the proposed framework to additional motor topologies.

## Acknowledgement

The authors would like to thank the Electric Machine and Drive System Laboratory of the Department of Electrical Engineering, NCKU, Taiwan, and Ansys for providing research facilities, software packages, and funding for this work. Additional gratitude is extended to UMY for partial funding support of this research project. Special thanks go to Muchammad Jamil for the contribution in 3D modeling design to the development of this work.

## References

[1] S. Leitman and B. Brant, *Build Your Own Electric Vehicle, 3rd Edition*. IEEE Electrical Insulation Magazine. New York: Mcgraw-Hill, 2014.

[2] A. Lordoglu, M. O. Gulbahce, and D.A. Kocabas, "A comprehensive disturbing effect analysis of multi-sectional rotor slot geometry for induction machines in electrical vehicles," *IEEE Access*, vol. 9, pp. 49590-49600, 2021. doi: 10.1109/ACCESS.2021.3068821

[3] M. Yilmaz, "Limitations/capabilities of electric machine technologies and modeling approaches for electric motor design and analysis in plug-in electric vehicle applications," *Renewable and Sustainable Energy Reviews*, vol. 52, pp. 80-99, 2015. doi: 10.1016/j.rser.2015.07.033

[4] M. İnci, M. Büyük, M. H. Demir, and G. İlbey, "A review and research on fuel cell electric vehicles: Topologies, power electronic converters, energy management methods, technical challenges, marketing and future aspects," *Renewable and Sustainable Energy Reviews*, vol. 137, 2021. doi: 10.1016/j.rser.2020.110648

[5] W. S. Jung, H. K. Lee, Y. K. Lee, S. M. Kim, J. I. Lee, and J. Y. Choi, (2023) "Analysis and Comparison of Permanent Magnet Synchronous Motors According to Rotor Type under the Same Design Specifications," *Energies*, vol. 16, no. 3, 2023. doi: 10.3390/en16031306

[6] B. Bilgin, J. Liang, M. V. Terzic, J. Dong, R. Rodriguez, E. Trickett, and A. Emadi, "Modeling and Analysis of Electric Motors: State-of-the-Art Review," *IEEE Transactions on Transportation Electrification*, vol. 5, no. 3, pp. 602-617, 2019. doi: 10.1109/TTE.2019.2931123

[7] J. F. Gieras, C. Wang, and J. C. Lai, *Noise of polyphase electric motors*. Boca Raton: Taylor & Francis, 2005.

[8] Y. Fang and T. Zhang, "Sound Quality of the Acoustic Noise Radiated by PWM-Fed Electric Powertrain," *IEEE Transactions on Industrial Electronics*, vol. 65, no. 6, pp. 4534-4541, 2018. doi: 10.1109/TIE.2017.2767558

[9] E. Król and M. Maciążek, "Identification and Analysis of Noise Sources of Permanent Magnet Synchronous Traction Motor with Interior Permanent Magnet," *Energies*, vol. 16, no. 16, 2023. doi: 10.3390/en16166018

[10] Z. Q. Zhu, Z. P. Xia, L. J. Wu, and G. W. Jewell, "Influence of slot and pole number combination on radial force and vibration modes in fractional slot PM brushless machines having single- and double-layer windings,' *2009 IEEE Energy Conversion Congress and Exposition (ECCE)*, 2009. doi: 10.1109/ECCE.2009.5316553

[11] S. Wu S, X. Yan, Z. Chen, Y. Zhang, and X. Feng, "New Rotor Topologies for Electromagnetic Forces and Acoustic Noise Reduction of claw Pole Alternators," *Journal of Electrical Engineering and Technology*, vol. 18, pp. 3751-3762, 2023. doi: 10.1007/s42835-023-01559-z

[12] J. W. Jung, S. H. Lee, G. H. Lee, J. P. Hong, D. H. Lee, and K. N. Kim, "Reduction design of vibration and noise in IPMSM type integrated starter and generator for HEV,' *IEEE Transactions on Magnetics*, vol. 46, no. 6, pp. 2454-2457, 2010. doi: 10.1109/TMAG.2010.2041434

[13] J. Cai and Z. Deng, "Offline and online modelling of switched reluctance motor based on RBF neural networks," *Journal of Electrical Engineering*, vol. 64, no. 3, pp. 186-190, 2013. doi: 10.2478/jee-2013-0027

[14] H. S. Nogay, "Deep convolutional neural networks for automatic coil pitches detection systems in induction motors," *Journal of Electrical Engineering*, vol. 72, no. 3, pp. 198-202, 2021. doi: 10.2478/jee-2021-0027

[15] M. F. Hsieh, L. H. Lin, T. A. Huynh, and D. Dorrell, "Development of Machine Learning-Based Design Platform for Permanent Magnet Synchronous Motor Toward Simulation Free," *IEEE Transactions on Magnetics*, vol. 59, no. 11, 2023. doi: 10.1109/TMAG.2023.3309151

[16] S. M. K. Zaman, X. Liang, and L. Zhang, "Greedy-gradient max cut-based fault diagnosis for direct online induction motors," *IEEE Access*, vol. 8, pp. 177851-177862, 2020. doi: 10.1109/ACCESS.2020.3027322

[17] M. Ertargin, O. Yildirim, and A. Orhan, "Mechanical and electrical faults detection in induction motor across multiple sensors with CNN-LSTM deep learning model," *Electrical Engineering*, vol. 106, pp. 6941-6951, 2024. doi: org/10.1007/s00202-024-02420-w

[18] M. Eker and B. Gündogan, "Demagnetization fault detection of permanent magnet synchronous motor with convolutional neural network," *Electrical Engineering*, vol. 105, pp. 1695-1708, 2023. doi: 10.1007/s00202-023-01768-9

[19] L. He, X. Wu, Y. Nie, and W. Shi, "Loss Prediction of Vehicle Permanent Magnet Synchronous Motor Based on Deep Learning," *Journal of Electrical Engineering and Technology*, vol. 18, 1053-1063, 2023. doi: 10.1007/s42835-022-01153-9

[20] X. Zhang, C. Li, M. Xue, W. Wang, and L. Zhu, "Application of Deep Learning in Motor Vibration and Noise Suppression Based on Negative Magnetostrictive Effect," *Journal of Electrical Engineering and Technology*, vol. 18, pp. 1931-1944, 2023. doi: 10.1007/s42835-022-01241-w

[21] T. Song, H. Liu, B. Bu, and Z. Zhang, "Rapid Calculation and Optimization of Vibration and Noise of Permanent-Magnet Synchronous Motors for EVs Based on Equivalent Structural Network," *Machines*, vol. 10, no. 4, pp. 281, 2022. doi: 10.3390/machines10040281

[22] Z. Hashemi, F. Zohrabi, and M. Mardaneh, "A Multi-objective Optimization of Switched Reluctance Motor using a Hybrid Analytic-ANFIS Model Considering the Vibrations," *Iranian Journal of Science and Technology, Transactions of Electrical Engineering*, vol. 43, pp. 361-371, 2019. doi: 10.1007/s40998-018-0093-1

[23] A. K. Sahu, A. Emadi, and B. Bilgin, "Noise and Vibration in Switched Reluctance Motors: A Review on Structural Materials, Vibration Dampers, Acoustic Impedance, and Noise Masking Methods," *IEEE Access*, vol. 11, pp. 27702-27718, 2023. doi: 10.1109/ACCESS.2023.3257124

[24] H. J. Shin, J. Y. Choi, H. I. Park, and S. M. Jang, "Vibration analysis and measurements through prediction of electro-magnetic vibration sources of permanent magnet synchronous motor based on analytical magnetic field calculations," *IEEE Transactions on Magnetics*, vol. 48, no. 11, 4216-4129, 2012. doi: 10.1109/TMAG.2012.2200658

[25] W. Zhang, Y. Xu, H. Huang, and J. Zou, "Vibration reduction for dual-branch three-phase permanent magnet synchronous motor with carrier phase-shift technique," *IEEE Transactions on Power Electronics*, vol. 35, no. 1, pp. 607-618, 2020. doi: 10.1109/TPEL.2019.2910311

[26] A. Malekipour, A. Corne, L. Garbuio, P. Granjon, and L. Gerbaud, "A Closed-Loop PMSM Sensorless Control Based on the Machine Acoustic Noise," *IEEE Transactions on Industrial Electronics*, vol. 70, no. 10, pp. 9859-9869, 2023. doi: 10.1109/TIE.2022.3206755

[27] R. M. Pindoriya, G. Gautam, and B. S. Rajpurohit, "A Novel Application of Pseudorandom-Based Technique for Acoustic Noise and Vibration Reduction of PMSM Drive," *2019 IEEE Industry Applications Society Annual Meeting*, 2019. doi: 10.1109/TIA.2020.2997904

[28] W. Deng and S. Zuo, "Electromagnetic vibration and noise of the permanent-magnet synchronous motors for electric vehicles: An overview," *IEEE Transactions on Transportation Electrification*, vol. 5, no. 1, pp. 59-70, 2019. doi: 10.1109/TTE.2018.2875481

[29] G. Park, C. Kim, M. Lee, and C. Choi, "Building geometry simplification for improving mesh quality of numerical analysis model," *Applied Sciences*, vol. 10, no. 16, 2020. doi: 10.3390/APP10165425

[30] M. Sosnowski, R. Gnatowska, K. Grabowska, J. Krzywański, and A. Jamrozik, "Numerical analysis of flow in building arrangement: Computational domain discretization," *Applied Sciences*, vol. 9, no 5, 2019. doi: 10.3390/app9050941

[31] L. Liu, J. Zhang, C. Song, C. Birk, and W. Gao, "An automatic approach for the acoustic analysis of three-dimensional bounded and unbounded domains by scaled boundary finite element method," *International Journal of Mechanical Sciences*, vol. 151, pp. 563-581, 2019. doi: 10.1016/j.ijmecsci.2018.12.018

[32] A. Johnen, J. C. Weill, and J. F. Remacle, "Robust and efficient validation of the linear hexahedral element," *Procedia Engineering*, vol. 203, pp. 271-283, 2017. doi: 10.1016/j.proeng.2017.09.809

[33] F. Mujaahid, M. F. Hsieh, T. Huda, M. Jamil, M. Y. Mustar, "Mesh Independence for Acoustic Noise of Permanent Magnet Synchronous Motor," *2023 International Workshop on Artificial Intelligence and Image Processing (IWAIIP)*, 2023. doi: 10.1109/IWAIIP58158.2023.10462759

[34] R. B. Randall, "A history of cepstrum analysis and its application to mechanical problems," *Mechanical Systems and Signal Processing*, vol. 97, pp. 3-19. doi: 10.1016/j.ymssp.2016.12.026

[35] Z. A. Haq and Z. A. Jaffery, "Impact of activation functions and number of layers on the classification of fruits using CNN," *2021 8th International Conference on Computing for Sustainable Global Development (INDIACom)*, 2021. doi: 10.1109/INDIACom51348.2021.00040

[36] X. Zhu, X. Zhao, J. Yao, W. Deng, H. Shao, and Z. Liu, "Adaptive Multiscale Convolution Manifold Embedding Networks for Intelligent Fault Diagnosis of Servo Motor-Cylindrical Rolling Bearing Under Variable Working Conditions," IEEE/ASME Transactions on Mechatronics, vol. 29, no. 3, pp. 2230-2240, 2024. doi: 10.1109/TMECH.2023.3314215

[37] M. Jing, G. Jia, and F. Zhang, "A permanent magnet motor winding fault diagnosis method based on image recognition and transfer learning," 2024 IEEE Transportation Electrification Conference and Expo, Asia-Pacific (ITEC Asia-Pacific), 2024. doi: 10.1109/ITECAsia-Pacific63159.2024.10738570

**Faaris Mujaahid** was born in Bandung, Indonesia. He received B.Eng. degree in electrical and electronic engineering from Saxion University of Applied Sciences, Enschede, the Netherlands, in 2010. He graduated from the University of Southampton, UK, M.Sc. program in Sustainable Energy Technologies in 2016. He is currently pursuing Ph.D. program at National Cheng Kung University (NCKU), Tainan, Taiwan. His research interests include electric motor design, deep learning, and renewable energy.

**Min-Fu Hsieh** (Senior Member, IEEE) received the B.Eng. degree in mechanical engineering from National Cheng Kung University (NCKU), Tainan City, Taiwan, in 1991, and the M.Sc. and Ph.D. degrees in mechanical engineering from the University of Liverpool, U.K., in 1996 and 2000, respectively. From 2000 to 2003, he was a researcher with the Electric Motor Technology Research Center, NCKU. In 2003, he joined the Department of Systems and Naval Mechatronic Engineering, NCKU, as an Assistant Professor. In 2012, he was promoted to a Full Professor. In 2017, he joined the Department of Electrical Engineering, NCKU, where he has been a Distinguished Professor since 2022. His research encompasses electric machine design, motor drives, and, more recently, AI/machine learning applications for electric machines. He serves as Associate Editor-in-Chief of IEEE Transactions on Magnetics, Associate Editor of IEEE Transactions on Industry Applications, and an IEEE Magnetics Society AdCom member (2026-2029) and Distinguished Lecturer (2025-2026). His conference leadership includes INTERMAG Publications Co-Chair and Local Organizing Committee Chair for the 2025 IEEE IAS Annual Meeting. An IET Fellow, he holds the Outstanding Research Award from Taiwan's National Science and Technology Council.

**Thorikul Huda** graduated from Institut Teknologi Sepuluh Nopember (ITS), Surabaya, Indonesia, with a Bachelor of Engineering (B.Eng.) and a Master of Engineering (M.Eng.) in Electrical Engineering. At National Cheng Kung University (NCKU) in Tainan, Taiwan, he is presently working toward a Ph.D. His areas of interest in research are artificial intelligence and electric motor control, with an emphasis on creating novel technologies and algorithms for AI-based motor control in a range of technological and industrial applications.

Received 16 February 2026